Atmos. Chem. Phys., 26, 16325–16340, 2026
https://doi.org/10.5194/acp-26-16325-2026
© Author(s) 2026. This work is distributed under
the Creative Commons Attribution 4.0 License.

Atmospheric Chemistry and Physics
Open Access
EGU

Research article

Vertical structure and controlling factors of cloud condensation nuclei activation over eastern China: Insights from aircraft measurements and interpretable machine learning

Yichen Lu[1], Honglei Wang[1,2], Deyu Liu[1], Yue Chen[1], Chong Peng[3], and Can Song[3]

[1]Collaborative Innovation Center on Forecast and Evaluation of Meteorological Disasters (CIC-FEMD), China Meteorological Administration Aerosol-Cloud and Precipitation Key Laboratory, Nanjing University of Information Science & Technology, Nanjing, China
[2]State Key Laboratory of Atmospheric Environment and Extreme Meteorology, Institute of Atmospheric Physics, Chinese Academy of Sciences, Beijing, China
[3]Weather Modification Centre of Henan Province, Zhengzhou, 450000, China

Correspondence: Honglei Wang (hongleiwang@nuist.edu.cn)

Received: 3 August 2026 – Discussion started: 6 August 2026
Revised: 8 November 2026 – Accepted: 10 November 2026 – Published: 17 November 2026

Abstract. Cloud condensation nuclei (CCN) play a critical role in cloud droplet formation and microphysical processes. Based on aircraft observations, this study investigated the factors controlling CCN number concentrations (NCCN) under different aerosol vertical structures (Decrease, Increase, and Stable, representing decreasing, increasing, and relatively stable aerosol concentrations with altitude, respectively) and supersaturation (SS) conditions using generalized additive models (GAM) combined with SHapley Additive exPlanations (SHAP).NCCN reached up to 10^3 cm^{-3} near the surface and generally decreased with altitude, while aerosol vertical structures modulated its abundance, with the Increase structure showing higher NCCN than Stable and Decrease structures. CCN activation ratios increased with SS and exhibited a non-monotonic vertical variation, with no consistent ranking among aerosol structures, indicating that supersaturation dominates CCN activation. Activated CCN droplet spectra showed unimodal distributions, with peak diameters increasing from ~ 2 µm at SS $= 0.2$ to ~ 5 µm at SS $= 1.0$. Although spectral shapes were similar among different structures, higher small-size aerosol concentrations (SA, 0.1–1 µm) were associated with higher CCN peak concentrations. GAM results identified several important explanatory variables for NCCN variations, with relative SHAP contributions of 19 %–57 % for temperature (T), 9 %–45 % for SA, 9 %–40 % for relative humidity (RH), and 3 %–32 % for horizontal wind speed (WS). SHAP analysis revealed that the contributions of T varied among different aerosol vertical structures, showing positive associations under Decrease and Increase structures but negative associations under Stable conditions, whereas SA consistently exhibited positive contributions. RH showed nonlinear relationships with NCCN, with an inflection point near 60 %.

Published by Copernicus Publications on behalf of the European Geosciences Union.

1 Introduction

Aerosols influence cloud droplet formation by acting as cloud condensation nuclei (CCN), representing one of the key pathways of aerosol–cloud–climate interactions (Guo and Xue, 2021; Köhler, 1936; Tao et al., 2021). Under certain supersaturation (SS) conditions, CCN can be activated to form cloud droplets, thereby affecting cloud droplet number concentration, effective radius, and microphysical structure, which in turn modify cloud radiative properties and precipitation efficiency. For instance, an increase in aerosols leads to higher CCN concentrations; if the cloud water content remains constant, this results in smaller droplet sizes, higher cloud droplet number concentrations, and increased cloud albedo (Lin et al., 2026; Twomey, 1977). Consistent with this classical response, aircraft observations over Hebei, China, have reported a negative relationship between aerosol loading and cloud droplet effective radius, with smaller droplets observed under more polluted conditions (Zhao et al., 2018). Reduced droplet collision–coalescence may also prolong cloud lifetime and suppress precipitation (Albrecht, 1989; Khatri et al., 2023). However, aerosol effects on precipitation are not universally suppressive. Under suitable thermodynamic and dynamical conditions, enhanced aerosol loading may invigorate convective development, modify latent-heat release and cloud dynamics, and potentially enhance precipitation. This aerosol invigoration effect further illustrates the strong dependence of aerosol–cloud–precipitation interactions on cloud regime and environmental conditions. These responses are commonly associated with the first and second aerosol indirect effects.

However, aerosol effects on clouds and precipitation are highly complex and depend on aerosol properties, cloud and precipitation regimes, the vertical distribution of aerosols, and meteorological conditions. Recent observational syntheses further indicate that aerosol perturbations may either suppress or enhance precipitation depending on the environmental and cloud dynamical context (Zhao et al., 2024). With the advancement of research, different and even contrasting aerosol–cloud responses have increasingly been reported. For example, Prabhakaran et al. (2026) found that under a warming climate, aerosol perturbations influence the stratocumulus-to-cumulus transition (SCT) over the northeastern Pacific; during the non-precipitating stratocumulus stage, the cloud radiative effect (CRE) responds more strongly to climate change than to aerosols, whereas aerosol effects become more important after cloud breakup. Khatri et al. (2022) reported that increased aerosol loading may enhance droplet collision–coalescence under certain conditions, leading to larger cloud droplets. Borys et al. (2003) observed that high anthropogenic aerosol concentrations substantially modified the microphysical structure of lower "feeder" layers in orographic clouds, suppressing or even inhibiting the riming growth of snow particles and thereby reducing snow water equivalent precipitation rates. These contrasting responses highlight the strong dependence of aerosol–cloud interactions on cloud type, aerosol characteristics, and environmental conditions. Therefore, a thorough understanding of CCN activation processes and the factors associated with their variability is crucial for improving our understanding of aerosol indirect climate effects.

The activation of CCN depends not only on ambient supersaturation but also on aerosol size distribution, chemical composition, and mixing state (Jose et al., 2026; Tao et al., 2021). In most atmospheric environments, particle size distribution is a decisive factor for CCN activation, with larger particles more readily activated at lower supersaturation (Asa-Awuku et al., 2008; Kleinheins et al., 2025). According to Köhler theory, the critical supersaturation of an aerosol particle is closely related to its size and hygroscopicity, which is strongly influenced by chemical composition; therefore, both aerosol size distribution and chemical composition are key determinants of CCN number concentration and activation characteristics. Moreover, aerosols and related environmental factors often exhibit pronounced vertical heterogeneity (Xu et al., 2022; Zhang et al., 2021) which may modulate CCN activation, yet the underlying mechanisms remain incompletely understood.

Current studies on CCN characteristics rely on a combination of ground-based observations, laboratory experiments, satellite retrievals, and aircraft measurements. Laboratory experiments provide controlled conditions for examining CCN activation as a function of aerosol size, chemical composition, hygroscopicity, and mixing state, whereas field observations are essential for characterizing CCN behavior under complex atmospheric conditions. Among these, aircraft observations uniquely provide vertical distributions of aerosols, meteorological variables, and cloud microphysical parameters, offering distinct advantages for investigating aerosol–cloud interactions. However, aircraft campaigns are generally limited in temporal and spatial coverage because of operational constraints, and individual flights may not fully capture seasonal variability, different synoptic regimes, or broader regional representativeness.

Aircraft observations over different regions of China have revealed pronounced vertical heterogeneity in CCN and aerosol properties. For example, Zhang et al. (2022) found that over the North China Plain, the vertical distribution of NCCN was jointly influenced by temperature (T) structure, air-mass origin, anthropogenic emissions, and topography. Xu et al. (2022) reported that in southern China, NCCN initially increased with altitude, peaked at approximately 1.3 km, and then decreased rapidly at higher levels. Liu et al. (2025) further showed that CCN vertical distributions were closely associated with boundary-layer structure, air-mass transport, and thermodynamic conditions, with aerosols at different altitudes potentially contributing to cloud droplet formation through vertical transport. These studies demonstrate the strong vertical variability of CCN over eastern and southern China and highlight the value of aircraft observa-

tions for resolving such structures. However, most previous studies have focused on overall vertical profiles or general statistical relationships, while systematic investigations of how different aerosol vertical structures, such as increasing, decreasing, or relatively stable profiles with altitude, influence CCN activation remain limited.

Traditional approaches, often based on correlation analysis or idealized theoretical frameworks, struggle to capture the nonlinear coupling among multiple factors. In recent years, machine learning (ML) has increasingly been applied in atmospheric sciences, showing clear advantages in handling high-dimensional, multivariate data and identifying key driving factors. In aerosol–cloud interaction studies, ML methods have been increasingly used to identify complex and nonlinear relationships among aerosol, cloud, and meteorological variables, particularly when multiple covarying environmental factors are involved (Chen et al., 2022). Their ability to handle high-dimensional datasets and nonlinear dependencies provides a useful complement to conventional statistical approaches. In studies of CCN number concentration and activation characteristics, ML methods have been applied to predict NCCN using aerosol physicochemical properties and meteorological variables, and to explore the relationships among aerosol composition, size distribution, and CCN activation (Ren et al., 2026; Nair et al., 2021). More recently, Ren et al. (2026) developed a machine-learning framework to predict NCCN at different supersaturation levels over the North China Plain across hourly-to-yearly timescales and employed SHAP analysis to interpret the relative importance of different predictors. Additionally, interpretable ML methods, such as SHAP, have been applied to quantitatively assess contributions of different factors to CCN and cloud microphysical parameters, providing critical insights into nonlinear mechanisms (Wang et al., 2025; Zipfel et al., 2024).

Against this background, the present study utilizes aircraft observations to investigate CCN activation characteristics under different aerosol vertical structures and environmental conditions sampled over eastern China. Interpretable statistical modeling is further employed to identify the major environmental factors associated with variations in CCN number concentration. The results provide vertically resolved observational evidence for understanding CCN variability under the atmospheric conditions sampled during the campaign and offer useful constraints for future studies of aerosol–cloud interactions.

2 Data and Methods

2.1 Overview of Aircraft Observations

This study utilized data from four aircraft flights, including one calibration flight conducted by B-3726 and three observation flights by B-3435. Among all flight missions, Flight 1 (F1) was conducted under clear-sky conditions, while Flights 2–4 (F2–F4) sampled mixed-phase clouds. In particular, the cloud base heights were approximately 2300 m in F3 and F4. Additional flight details are provided in Table 1.

As shown in Fig. 1, after taking off from Zhengzhou, F2 sampled altitudes between 1800 and 4500 m, with in-cloud measurements around 4000 m (cloud identification criteria are detailed in Sect. 2.3). F3 sampled altitudes from 2400 to 4200 m, with limited in-cloud data obtained around 2300 m. During F4, the sampling altitude ranged from 2200 to 6000 m, where relatively deep clouds were observed.

2.2 Instruments and Data Processing

The observations in this study were obtained using a Cloud Condensation Nuclei Counter (CCNC), Cloud Droplet Probe (CDP), Cloud Imaging Probe (CIP), Passive Cavity Aerosol Spectrometer Probe (PCASP), and the 20 Hz Aircraft Integrated Meteorology Measuring System (AIMMS-20). The core of the CCNC is a cylindrical thermal gradient diffusion chamber. A constant T gradient is applied along the walls of the chamber. Since heat diffuses more slowly through the air than through water vapor, a supersaturation is produced inside the cylinder. Aerosol flow is introduced into the centerline of the filtered and humidified sheath flow. A constant ratio of 10 : 1 is maintained between the sheath and aerosol flow. Supersaturation is developed inside the chamber according to the chamber flow, the streamwise T gradient, and the absolute pressure inside the column. Those particles whose critical supersaturation is less than the instrument supersaturation will grow as cloud droplet (Jayachandran et al., 2017; Liu et al., 2020). Five supersaturation levels (0.2 %, 0.4 %, 0.6 %, 0.8 %, and 1.0 %) were set in the experiment. Each measurement cycle lasted 25 min, with a sampling time of 5 min at each supersaturation level. Because these supersaturation levels were measured sequentially rather than simultaneously, the aircraft altitude could change during a complete measurement cycle, resulting in partial coupling between sampling altitude and supersaturation. Therefore, measurements at each supersaturation level were analyzed according to the altitude at which they were actually obtained, and comparisons among different supersaturation levels were interpreted with caution. Since the CCNC requires a finite response time to reach a stable supersaturation after switching between different supersaturation settings, transient periods around supersaturation transitions were excluded. The first and last 60 s of each supersaturation period were removed, and only the stable measurement period was retained for subsequent analysis(Jayachandran et al., 2017; Lance et al., 2006). The CDP provides comprehensive information on cloud droplet number concentration, size distribution, and liquid water content for droplets ranging from 2 to 50 µm (Faber et al., 2018). By guiding cloud droplets into the probe, the CDP determines the diameter of individual liquid droplets based on single-particle light scattering principles (Ke et al., 2024). The CIP quantifies ice particle concentration (N_i) and particle morphology by imaging

Table 1. Overview of aircraft flight missions, including aircraft models, flight dates and takeoff times, cloud phases, 0 °C-level altitudes, and departure locations.

Flight	Aircraft Model	Date	Takeoff Time (UTC+8)	Cloud Phase	0 °C Level Altitude	Departure Location
1	B-3726	31 March 2018	21:44	Clear-sky	–	–
2	B-3435	23 March 2018	20:48	Mixed-phase	3500 m	Zhengzhou
3	B-3435	24 March 2018	13:55	Mixed-phase	2600 m	Xinzheng Airport
4	B-3435	26 March 2018	16:00	Mixed-phase	3100 m	Xinzheng Airport

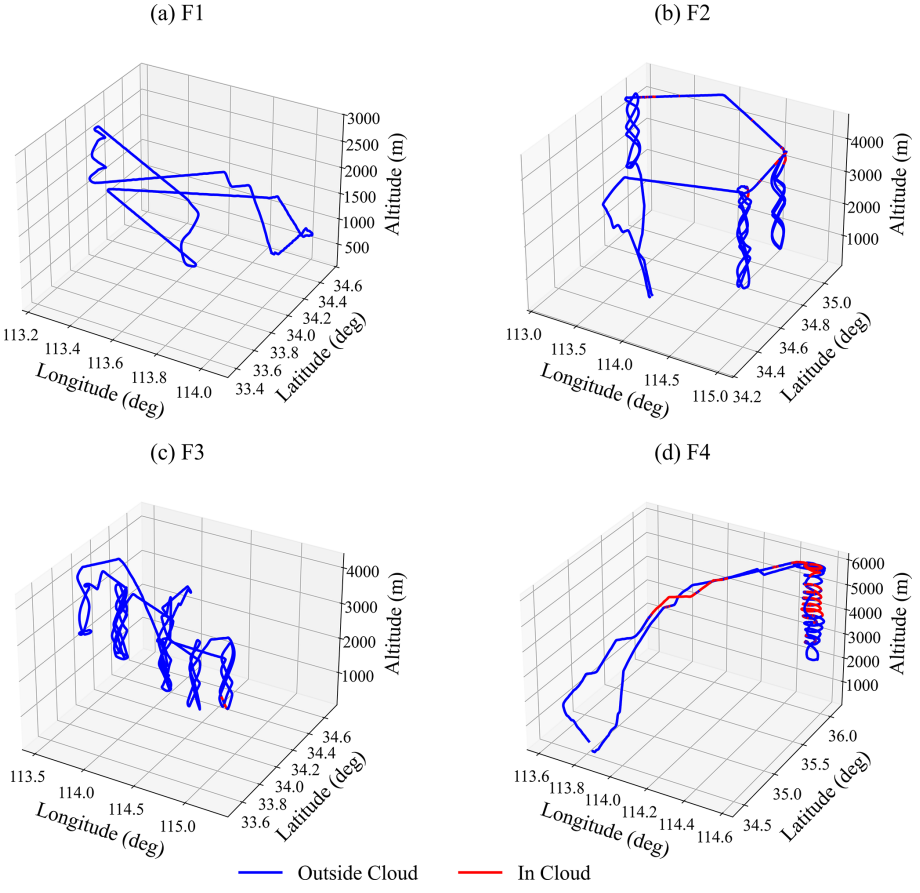

Figure 1. Flight trajectories of the four aircraft observation missions over eastern China (F1–F4 correspond to 21, 23, 24, and 26 March, respectively). Blue and red segments indicate flight portions outside and inside clouds, respectively.

particles passing through a collimated laser beam (Baumgardner et al., 2001). The PCASP measures particle size distribution based on the intensity of scattered light generated as individual particles pass through a laser beam, using the known relationship between scattering intensity and particle diameter (Cai et al., 2013). AIMMS-20 is a meteorological measurement system that provides integrated and on-demand atmospheric data (Ke et al., 2024). Measurement uncertainties were considered in the interpretation of the observations. For the CCNC, the main uncertainty is associated with supersaturation calibration (Rose et al., 2008). For the PCASP and CDP, particle sizing may be affected by calibration and refractive-index assumptions (Rosenberg et al., 2012; Faber et al., 2018), while CIP measurements may additionally be influenced by ice-particle shattering and image-processing uncertainties (Lawson, 2011). Detailed instrument specifications are provided in Table 2.

In this study, the number concentrations of CCN (NCCN), cloud droplets (N_c), ice crystals (N_i), and aerosols (N_a) were obtained by summing the particle number concentrations across the corresponding instrument channels. This summation is equivalent to integrating the measured particle size distribution, $n(r)$, over the corresponding particle-size range.

Table 2. Summary of aircraft-borne instruments and their measurement specifications, including measured variables, measurement ranges, temporal resolutions, channels/bins, and manufacturers.

Instrument	Measured Variables	Measurement Range	Temporal Resolution	Channels /Bins	Manufacturer
CCNC	CCN number concentration (NCCN), activated droplet size distribution	0.75–10 µm	1 s	20	Droplet Measurement Technologies (DMT)
CDP	Cloud droplet size distribution	2–50 µm	1 s	30	Droplet Measurement Technologies (DMT)
CIP	Cloud particle size distribution	25–1550 µm	1 s	62	Droplet Measurement Technologies (DMT)
PCASP	Aerosol size distribution	0.1–3 µm	1 s	30	Droplet Measurement Technologies (DMT)
AIMMS-20	Meteorological variables (T, RH, etc.)	–	1 s	–	Advanced Airborne Measurement Solutions

The resulting number concentrations are expressed in cm^{-3} for NCCN, N_c, and N_a, and in L^{-1} for N_i.

To reduce the uncertainty associated with the smallest particle sizes, the first two CIP size bins were excluded when calculating N_i. The CIP-derived N_i was used primarily to support in-cloud identification rather than to analyze detailed ice-particle size distributions. No dedicated shattering correction was applied, and the potential influence of residual shattering artifacts is therefore acknowledged.

2.3 In-Cloud Data Classification

Based on previous airborne cloud microphysical studies (Hobbs and Rangno, 1998; Hou et al., 2021; Lance et al., 2010) and operational experience from weather-modification aircraft observations in China, a conservative in-cloud screening criterion was adopted. Because the purpose of cloud identification in this study was not to distinguish cloud phase but to exclude observations potentially affected by cloud particles, a measurement was considered in-cloud when either $N_c \geq 10\,cm^{-3}$ or $N_i > 1\,L^{-1}$.

During in-cloud measurements, the CCN counter may detect both activated cloud droplets and interstitial aerosol particles. Without dedicated instrumentation or specific correction procedures, these two particle populations cannot be reliably distinguished. Therefore, to minimize the influence of cloud droplet activation on the CCN measurements, all data identified as in-cloud according to the criteria described above were excluded from subsequent analyses.

2.4 GAM and SHAP

GAM are flexible regression models that account for the additive effects of predictor variables on the response, including their potential nonlinear relationships (Bi et al., 2022). By applying smooth functions to input features, GAM can effectively capture nonlinear dependencies. In meteorology and atmospheric sciences, GAM is widely used to model complex environmental data and can accurately describe the relationships between meteorological variables and atmospheric constituents (Annareddy et al., 2026). GAM were selected in this study because the primary objective was to quantify the nonlinear relationships between environmental factors and CCN activation rather than simply maximize predictive performance. Unlike some complex machine learning and deep learning approaches that primarily emphasize predictive performance and may suffer from limited interpretability, GAM provides an interpretable framework by describing the response variable as the sum of smooth functions of individual predictors. This characteristic allows us to identify the nonlinear response patterns and potential thresholds of CCN concentrations in response to meteorological conditions and aerosol properties. SHAP is a framework for interpreting predictions from complex models, assigning an importance value to each feature to help understand why a model produces a specific prediction (Lundberg and Lee, 2017). SHAP is based on the Shapley value concept from game theory, which extracts feature contributions to ensure fair and consistent explanations. In this study, GAM was combined with SHAP to analyze the relationships between meteorological factors, cloud microphysical properties, and CCN concentrations.

To reduce multicollinearity among aerosol variables, total aerosol number concentration (N_a) was excluded, whereas small-size aerosol number concentration (SA, 0.1–1 µm), medium-size aerosol number concentration (MA, 1–2 µm), and large-size aerosol number concentration (LA, 2–3 µm) were retained to represent size-resolved aerosol populations, thereby improving interpretability and avoiding redundancy. The dataset was randomly divided into training (80 %) and testing (20 %) sets using a fixed random seed (random_state = 42). To improve model robustness and re-

duce the risk of overfitting, a backward stepwise elimination procedure was incorporated into the GAM framework. At each iteration, p-values were examined, with a significance threshold of 0.01 used to guide the elimination procedure. The AIC was recorded for each candidate model, and the model with the lowest AIC across all iterations was selected as the final model. Model performance was evaluated using R^2.

For nonlinear interpretation, SHAP values were computed using a model-agnostic Kernel Explainer applied to the trained GAM. A background dataset of 100 training samples and 300 test samples were used for Monte Carlo-based approximation of feature contributions. Two SHAP metrics were used in this study: the mean absolute SHAP value, representing global feature importance, and the mean signed SHAP value, indicating the direction of each feature's impact on CCN concentration. The SHAP contribution percentage was calculated by normalizing the mean absolute SHAP values across all features.

To assess the influence of temperature–altitude coupling inherent in aircraft observations, an additional sensitivity analysis was conducted. First, the temperature–altitude relationship was quantified for the full cloud-free dataset using Pearson and Spearman correlation coefficients, both for the combined dataset and for the three aerosol vertical-structure categories. Second, a near-constant-altitude flight segment around 5.8 km was selected, where altitude variability was small while temperature still exhibited measurable variation. For each SS level, summary statistics of altitude, temperature, and CCN concentration were calculated, and temperature–altitude correlations were evaluated. Based on the sample size, temperature variability, and altitude stability, the SS = 0.6 % subset was selected for the GAM/SHAP sensitivity analysis. The results from this subset were then compared with those obtained from the full dataset.

To quantify the uncertainty in the SHAP-based relative contribution percentages, a nonparametric bootstrap analysis was further performed using the sample-level SHAP values from the original analysis. For each aerosol vertical-structure and supersaturation scenario, observations and their corresponding SHAP-value vectors were resampled with replacement 1000 times. For each bootstrap replicate, the mean absolute SHAP value of each predictor was recalculated and normalized by the sum across all predictors. The 2.5th and 97.5th percentiles of the resulting bootstrap distributions were taken as the lower and upper bounds of the 95 % confidence intervals, respectively.

3 Results and Discussion

3.1 Influence of Different Aerosol Vertical Structures on CCN Vertical Profiles

Figure 2 summarizes the vertical distributions of meteorological variables and particle concentrations during the four flight missions. T generally decreased with altitude, and no T inversion layer was observed. Near-surface T during F2–F4 exceeded 15 °C, whereas F1 exhibited relatively lower T of approximately 10 °C. Relative humidity (RH) generally increased with altitude in the lower atmosphere and decreased at higher levels, although F2 showed a more complex structure, with RH decreasing near 2000 m and increasing again around 2700 m. Horizontal wind speed (WS) generally increased with altitude above 2000 m, while greater variability was observed below this level. Vertical wind speed (VW) measurements indicated predominantly downward motions below 1000 m and stronger fluctuations aloft.

N_a was highest near the surface, reaching the order of 10^4 cm^{-3}, and generally decreased with altitude (Figs. 2e and S3–S6 in the Supplement). Elevated N_c and N_i were observed in several flight missions. For example, F2 exhibited enhanced N_c and N_i near 4500 m, consistent with the cloud events identified around 21:30 and 22:00 LT (Fig. S4). Similar enhancements were also observed during F3 and F4 (Figs. 2f, g and S5–S6), indicating the presence of cloud layers at different altitudes. According to the cloud classification criteria described in Sect. 2.3, these observations were used to identify in-cloud periods, which were subsequently excluded from the CCN analysis.

Figures 2h and S1 in the Supplement show that CCN number concentration (NCCN) reached values on the order of 10^3 cm^{-3} near the surface and generally exhibited decreasing vertical profiles under different supersaturation (SS) conditions, although local increases and nearly constant layers were also observed. For example, under SS = 0.4 %, the NCCN profile during F1 exhibited a decrease–increase–decrease pattern with altitude. When observations from all flight missions were grouped by altitude and analyzed separately for each SS level (Fig. S2 in the Supplement), CCN activation ratios generally exhibited an increase–decrease–increase pattern with altitude, although local deviations from this overall tendency were present. At SS = 0.2 % and 0.6 %, activation ratios generally increased below approximately 2000 m, decreased toward ∼ 4000 m, and then increased again at higher altitudes. A similar pattern was observed at SS = 0.4 %, with the transition from increasing to decreasing occurring near ∼ 1500 m. At higher SS, the initial increasing tendency extended to higher altitudes, reaching approximately 2500 m at SS = 0.8 % and ∼ 3000 m at SS = 1.0 %, followed by a decrease toward ∼ 4000 m and a subsequent increase above this level. Relatively low activation ratios were observed around 4000 m in the composite profiles (3 %–8 % for SS ≤ 0.6 % and 21 %–35 % for SS > 0.6 %). Overall, activation ratios under SS ≥ 0.8 % were higher than those under lower supersaturation conditions. It should be noted that the CCNC operated sequentially across different supersaturation levels during each flight, resulting in partial coupling between altitude and supersaturation. Therefore, the vertical variations presented here represent composite statistics based on the observations available at each

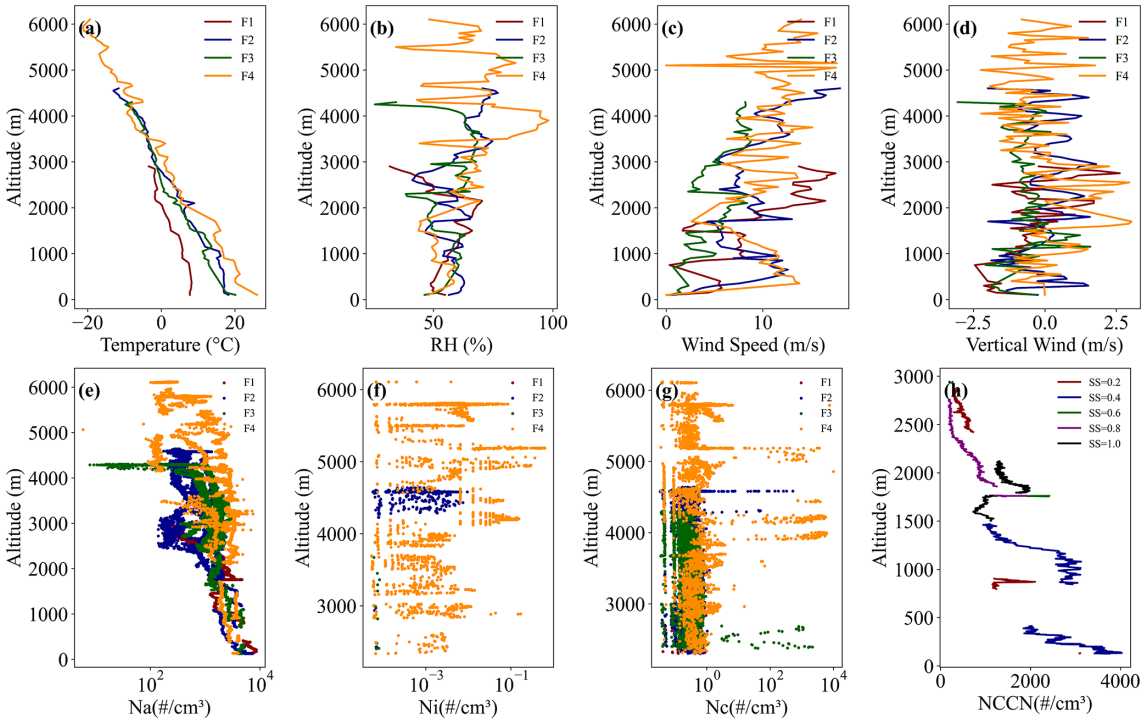

Figure 2. Vertical profiles of meteorological variables and particle concentrations for different flight missions. **(a)** Temperature; **(b)** Relative humidity; **(c)** Horizontal wind speed; **(d)** Vertical wind speed; **(e)** Aerosol number concentration; **(f)** Ice crystal number concentration; **(g)** Cloud droplet number concentration; **(h)** Variation of CCN number concentration with height under different supersaturation conditions during F1. Different colors represent different flight missions (F1–F4).

SS level rather than strictly altitude-controlled comparisons among supersaturation conditions. Accordingly, differences among SS levels may partly reflect variations in sampling altitude and flight trajectory and should be interpreted with appropriate caution.

To investigate the impact of aerosol vertical structure on CCN activation characteristics, aerosol number concentration profiles were divided into consecutive vertical trend segments according to changes between adjacent altitude bins (Fig. S7 in the Supplement). The classification thresholds were empirically determined from the present observational dataset based on the distribution of aerosol number concentration and visual inspection of the vertical profiles. Specifically, adjacent bins were classified as Stable when the absolute difference in aerosol number concentration was $< 100\,\mathrm{cm}^{-3}$ and the relative change was $< 20\,\%$, which was intended to distinguish relatively small fluctuations from more pronounced vertical trends. Changes exceeding these thresholds were classified as Increase or Decrease according to the direction of the change. The resulting segments were subsequently grouped into the three aerosol vertical structure categories.

The statistical characteristics of NCCN and activation ratio under different aerosol vertical structure categories are further examined using boxplot analysis (Figs. 3 and S8 in the Supplement). The results show that NCCN exhibits generally higher median and mean values in the Increase category compared with the Stable and Decrease categories across most supersaturation conditions, indicating that aerosol vertical structure may influence the overall abundance of CCN. In contrast, CCN activation ratios show a strong dependence on supersaturation, with generally higher values under $\mathrm{SS} \geq 0.8\,\%$ compared to lower supersaturation conditions. However, differences among aerosol vertical structure categories are not consistently ordered across all SS levels, suggesting a condition-dependent rather than systematic structural control. Moreover, the interquartile range of activation ratios decreases with increasing supersaturation, indicating reduced variability and a more constrained activation state under high-SS conditions.

Figure 4 shows that the size distributions of CCN-activated droplets measured by the CCNC are generally dominated by a main mode, although a small-particle shoulder below $\sim 2\,\mu\mathrm{m}$ is apparent under some low-SS conditions. The dominant modal diameter is approximately 2–3 µm at low SS (0.2 % and 0.4 %) and shifts toward $\sim 5\,\mu\mathrm{m}$ at higher SS (0.8 % and 1.0 %). The reduced prominence of the small-particle shoulder and the shift toward larger diameters at higher SS are consistent with enhanced condensational growth of activated droplets within the CCNC, rather than changes in the critical activation diameter of aerosol particles. Under higher SS conditions, smaller aerosol particles

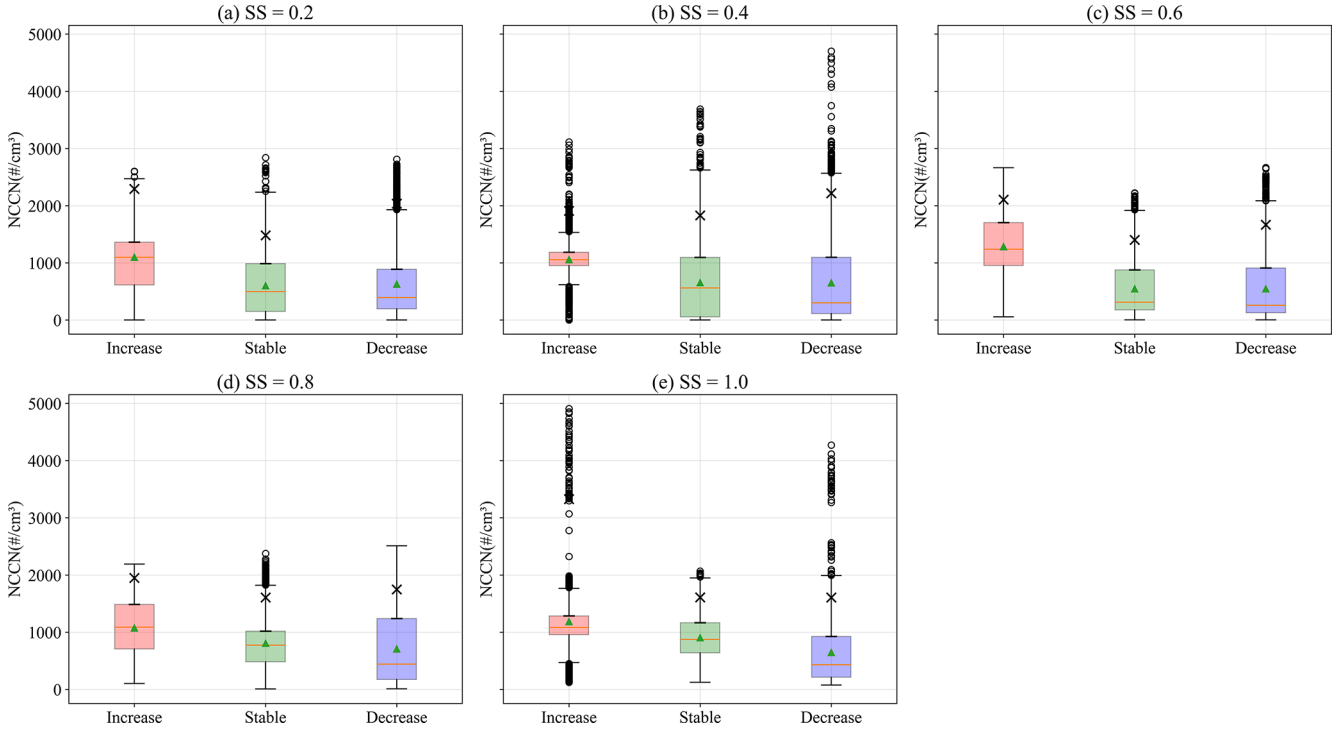

Figure 3. Distribution of cloud condensation nuclei (CCN) concentrations under different supersaturation (SS) conditions and aerosol vertical structural regimes. Boxplots illustrate CCN number concentrations (CCN NC) for three aerosol vertical structures (increasing, stable, and decreasing types) across five supersaturation levels (SS = 0.2, 0.4, 0.6, 0.8, and 1.0). The central line in each box represents the median value, while the box denotes the interquartile range (25th–75th percentiles). Whiskers extend to 1.5 times the interquartile range, and black circles indicate outliers. The triangle markers represent the arithmetic mean CCN concentration for each group. In addition, the 75th percentile (horizontal line) and 95th percentile (cross marker) are explicitly shown to highlight upper-tail behavior and distribution asymmetry under different aerosol structural and supersaturation conditions.

can also be activated, while stronger water vapor supersaturation promotes faster condensational growth after activation. For instance, in F1 (Fig. 4a–e), the modal diameter at SS = 0.2 % is approximately 2 µm for all three aerosol vertical structures, whereas at SS = 1.0 % it increases to 5.5, 5.5, and 4.5 µm for the Increase, Stable, and Decrease structures, respectively.

CCN-activated droplet spectra exhibit similar shapes among different aerosol vertical structures, with only minor differences in modal diameters and peak concentrations. For example, in Fig. 4q, the modal diameter is 2 µm for all three structures, with peak concentrations of 982, 646, and 519 cm^{-3} μm^{-1} for the Increase, Stable, and Decrease structures, respectively. However, differences in CCN peak concentrations are not consistent among all cases. In Fig. 4b, the Decrease structure exhibits the highest peak concentration, while the Stable structure shows the lowest; in contrast, the opposite pattern is observed in Fig. 4s.

To further investigate the influence of vertical structure, the corresponding aerosol size distributions were analyzed (Fig. S9 in the Supplement, The corresponding particle size distributions plotted on a logarithmic diameter scale are provided in Fig. S34 in the Supplement.). Aerosol spectra generally exhibit a unimodal distribution consistent with the CCN-activated droplet spectra, with a peak around 0.14 µm, followed by a rapid decline beyond 0.32 µm. High concentrations of aerosols with diameters < 1 µm correspond to higher CCN peak concentrations. For example, in Fig. S9p, the < 1 µm aerosol concentration follows the order Increase > Decrease > Stable, which is consistent with the corresponding CCN-activated droplet spectra in Fig. 4p Similar patterns are observed in other cases, suggesting that variations in < 1 µm aerosol concentrations likely contribute to changes in CCN peak concentrations.

It should be noted that the CCN-activated droplet sizes measured by the CCNC reflect a continuous condensational growth process under prescribed supersaturation conditions, rather than an equilibrium particle size. Therefore, the retrieved droplet sizes may be sensitive to instrumental settings, CCN concentration, and water vapor supply conditions, and interpretations of size-related variations should be made with appropriate caution. Overall, the results indicate that CCN vertical distributions are jointly regulated by supersaturation, aerosol loading, and vertical structural characteristics. Supersaturation primarily controls the activation efficiency, resulting in consistently higher activation

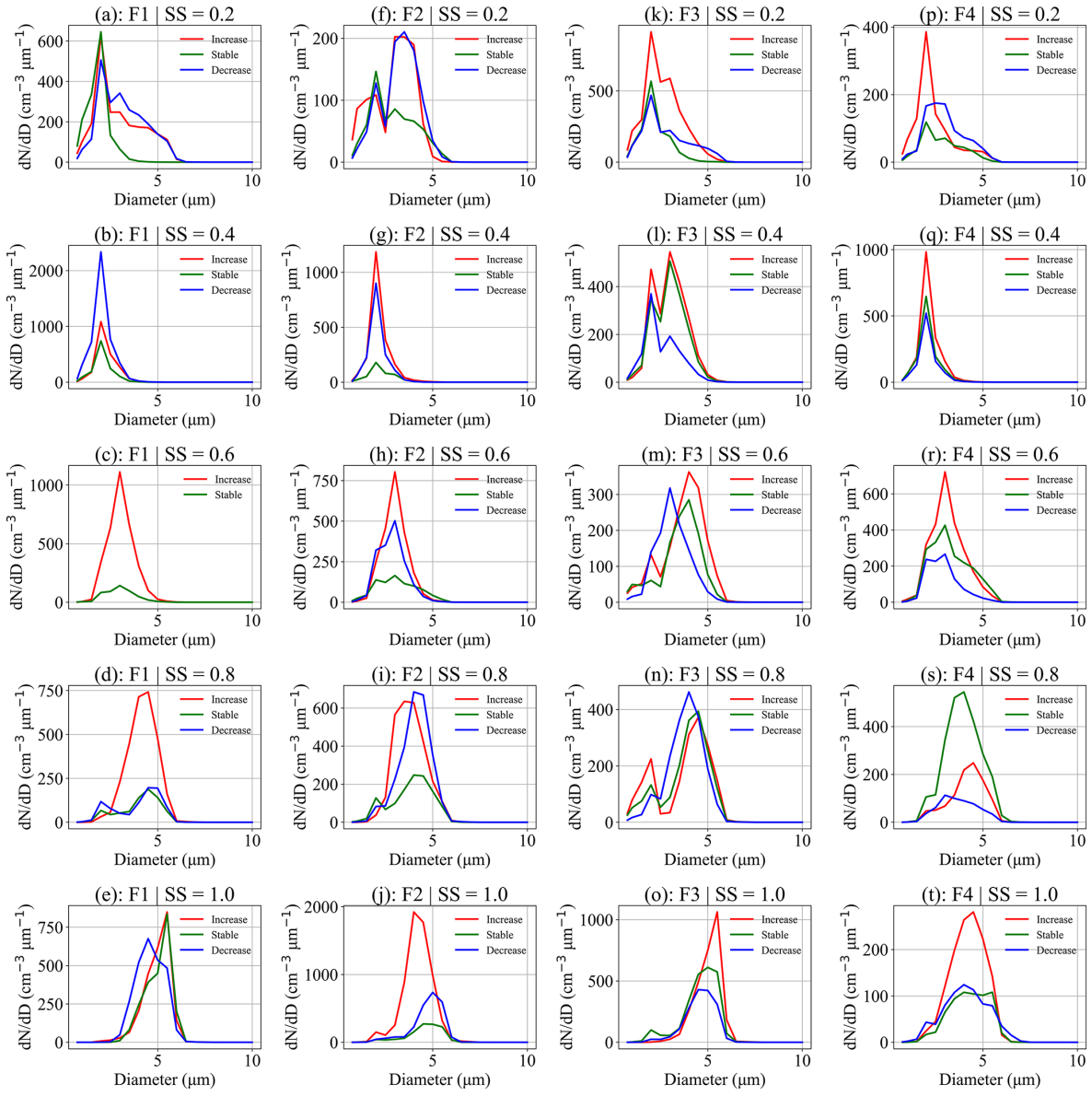

Figure 4. Size distributions of activated droplets measured by the CCNC under different supersaturation (SS) conditions and aerosol vertical structures for Flights F1–F4. Columns represent individual flight missions, and rows correspond to different SS conditions. Red, green, and blue curves denote the Increase, Stable, and Decrease aerosol vertical structures, respectively.

ratios under high-SS conditions, while aerosol vertical structure mainly modulates CCN availability through variations in aerosol abundance, particularly submicron particles.

However, the influence of vertical structure on activation ratios is not systematic across all supersaturation levels, suggesting a strong condition-dependent behavior rather than a purely structural control. These results further imply that CCN variability arises from coupled effects between aerosol population characteristics and environmental conditions, rather than a single dominant factor. This motivates a more quantitative investigation of the relative roles of meteorological conditions and size-resolved aerosol properties in CCN formation, which is further addressed using correlation analysis, GAM modeling, and SHAP-based interpretation in the following sections.

3.2 Correlation Analysis between CCN Number Concentration and Environmental Factors under Different Supersaturation Conditions

Pearson correlation analysis was conducted to quantify the relationships between CCN number concentrations and environmental factors under different aerosol vertical structures and supersaturation conditions. Statistical significance was

assessed using p-values, and correlation coefficients were reported to evaluate the strength and direction of these relationships. Figure 5 shows that, across different aerosol vertical structures, T, SA, and N_a are generally positively correlated with CCN concentrations, whereas WS, VW, MA, and LA exhibit predominantly negative correlations. RH shows an SS-dependent relationship, with negative correlations under low supersaturation conditions (SS = 0.2 and 0.4) but positive correlations at higher supersaturations (SS = 0.6, 0.8, and 1.0). Among all examined factors, T, SA, and N_a exhibit the strongest correlations with CCN, followed by RH and WS, while VW, MA, and LA show relatively weaker relationships.

The overall correlation patterns are generally consistent among different aerosol vertical structures, although the correlation coefficients vary. In particular, correlations under the Stable structure are generally weaker than those under the Increase and Decrease structures. For example, T exhibits positive correlations with CCN under all three structures, with mean correlation coefficients of 0.456, 0.672, and 0.666 for Stable, Increase, and Decrease structures, respectively. Furthermore, relatively high correlation coefficients in the Increase structure mainly occur at SS = 0.2, 0.8, and 1.0, whereas those in the Decrease structure are primarily observed at SS = 0.8 and those in the Stable structure at SS = 0.4.

Notably, the correlations between N_a and CCN are highly consistent with those between SA and CCN, with differences in correlation coefficients generally within 0.1. This suggests that variations in N_a are largely associated with changes in SA, highlighting the importance of small-size particles in determining aerosol number concentration variability. This result is also consistent with the aerosol size distribution characteristics shown in Fig. S9.

3.3 Quantitative Analysis of Factors Influencing CCN Activation Based on GAM and SHAP Machine Learning Approaches

To further investigate the nonlinear effects of these factors on CCN number concentration and quantify their individual contributions, a GAM was employed in combination with the SHAP method. This approach enables the assessment of the relative importance of each factor and elucidates their underlying mechanisms. Model evaluation results indicate that the mean R^2 values for the training and test sets are 0.85 and 0.82, respectively, demonstrating good model fit and generalization performance. The relationship between predicted and observed NCCN values (Fig. S10 in the Supplement) shows that most data points are distributed near the 1 : 1 reference line, indicating strong agreement between model predictions and observations, consistent with the high R^2 values.

Figure 6 shows that T, RH, WS, and SA generally exhibit relatively high SHAP contributions across the three aerosol vertical structures, although their relative importance varies with supersaturation and aerosol structure. Specifically, T is the dominant predictor across all SS levels under the Decrease and Stable structures, with relative SHAP contributions consistently exceeding approximately 29 %. Under the Increase structure, the relative importance of T decreases under some SS conditions but remains above approximately 19 %, indicating that T remains an important explanatory variable for NCCN variability within the model framework. RH contributes approximately 17 % on average and reaches nearly 40 % under certain conditions. WS contributes approximately 12 % on average and reaches ∼ 32 % under SS = 0.6 % in the Increase structure, indicating strong scenario dependence. These associations may partly reflect the roles of humidity in aerosol hygroscopic growth and horizontal wind in aerosol transport and dispersion, although the SHAP results themselves do not imply direct causal effects. SA also generally exhibits high relative SHAP contributions across most scenarios, frequently exceeding 15 %. Bootstrap-derived 95 % confidence intervals further indicate that these broad feature-importance patterns are generally robust, although the intervals overlap for several predictors with similar contributions, suggesting that small differences in their exact rankings should not be overinterpreted (Table S1 in the Supplement).

In contrast, VW contributes less than 10 %, indicating a relatively minor impact on NCCN. MA and LA also contribute less than 10 %, much lower than SA, suggesting that the contribution of aerosols to NCCN is primarily driven by SA, consistent with previous analyses.

Moreover, the SHAP net contributions of NCCN exhibit notable differences under varying aerosol vertical structures and supersaturation conditions (Fig. S11 in the Supplement). The net contributions of T, RH, WS and SA generally have larger absolute values, whereas those of VW, LA and MA are relatively smaller, consistent with the previously discussed contribution rates. Specifically, T shows predominantly positive contributions under the Decrease and Increase scenarios, but mainly negative contributions under the Stable scenario. SA contributes positively across all three scenarios, while the directions of WS and RH contributions do not show clear scenario-dependent patterns.

In summary, the model identifies T (20 %–56 %), SA (9 %–45 %), RH (9 %–40 %), and WS (3 %–32 %) as the most important factors under most scenarios, whereas LA, MA, and VW only show significant contributions in specific cases. Analysis of the individual SHAP value variations (Figs. S12–S29 in the Supplement) further reveals that, the SHAP values of T, RH, WS, VW, and SA generally exhibit pronounced nonlinear behavior across different scenarios, while those of LA and MA vary approximately linearly.

The contribution of T generally increases with its magnitude; in the high range, it usually shows positive SHAP values, whereas in the low range it shows negative SHAP values. This indicates that the model considers higher T conditions favorable for an increase in NCCN, while lower T condi-

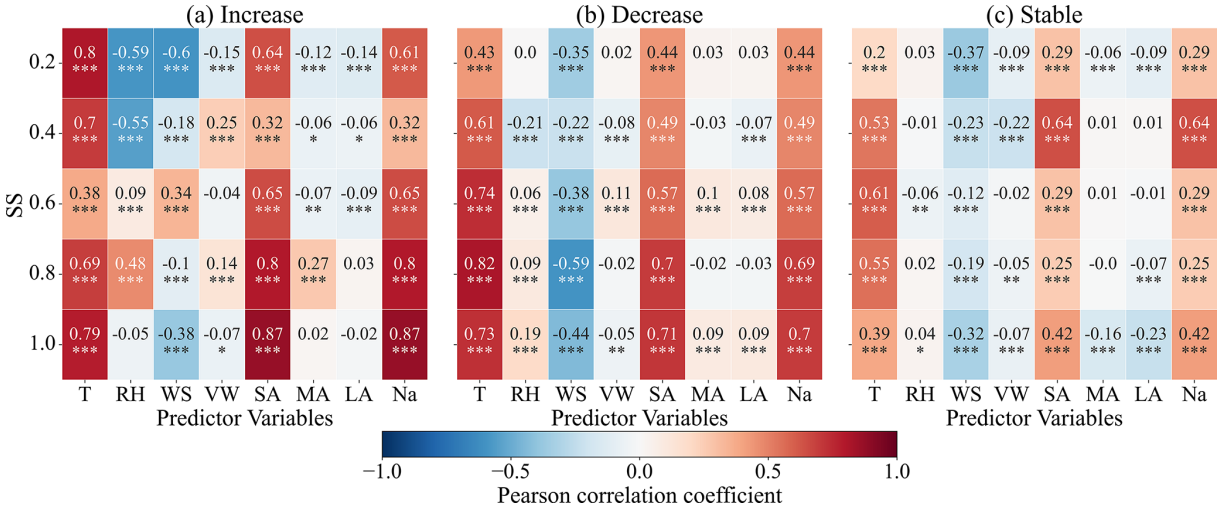

Figure 5. F1–F4 Correlation between CCN number concentration and various environmental factors under different aerosol vertical structures for Flights F1–F4 at multiple supersaturation (SS) conditions. Four meteorological variables and four aerosol size classes are included: small aerosols (SA, 0.1–1 µm), medium aerosols (MA, 1–2 µm), large aerosols (LA, 2–3 µm), and total aerosols (N_a, 0.1–3 µm). Red and blue colors indicate positive and negative correlations, respectively, and the numerical values represent the correlation coefficients. Asterisks denote statistical significance (* $p < 0.05$, ** $p < 0.01$, *** $p < 0.001$).

tions are unfavorable. Comparing the vertical distributions of T and N_a (Figs. 2 and S7) reveals a certain similarity: high (low) T values often correspond to higher (lower) N_a concentrations. Therefore, the contribution of T to NCCN in the model may partly reflect the coordinated variation between T and N_a distributions, rather than implying that T alone directly controls CCN formation.

Because temperature and altitude are physically linked in aircraft observations, we further evaluated the robustness of the temperature–NCCN relationship through a sensitivity analysis. In the full cloud-free dataset, temperature was strongly negatively correlated with altitude, with Pearson $r = -0.950$ and Spearman $\rho = -0.954$ (Fig. S30 in the Supplement). Similar negative correlations were found within the Increase, Stable, and Decrease structure categories, although the correlation strength varied among them. These results indicate that the high importance of temperature in the full-dataset GAM/SHAP analysis should be interpreted with caution.

To further examine the temperature–NCCN relationship under conditions of limited altitude variability, a near-constant-altitude flight segment near 5.8 km was analyzed. In this segment, the altitude range was only 10–17 m depending on supersaturation level, whereas temperature still varied by approximately 0.9–2.3 °C. The temperature–altitude correlations within these subsets were substantially weaker and no longer systematically negative, indicating that the original large-scale coupling was considerably mitigated. The SS = 0.6 % subset used for the GAM/SHAP sensitivity analysis comprised 506 samples and covered a temperature range of 2.27 °C. In this near-constant-altitude subset, the relative SHAP importance of temperature decreased compared with that in the full dataset (Fig. S32 in the Supplement), but the SHAP dependence still showed an overall increase with temperature (Fig. S33 in the Supplement). This suggests that altitude-related covariation explains part, but not all, of the temperature importance identified in the full dataset. Nevertheless, this result should still be interpreted as a statistical association rather than a direct causal temperature effect.

The contribution of SA generally increases with its magnitude, showing a significant positive effect on NCCN at high values. This may be because small particles can grow through condensation or coagulation into the accumulation mode, becoming effective cloud condensation nuclei. Previous studies have shown that small particles produced by new particle formation can significantly increase CCN concentrations during subsequent growth (Kerminen et al., 2012). Therefore, an increase in SA may reflect an enhanced potential source of CCN, resulting in a positive contribution in the model.

The SHAP values of RH exhibit a pronounced nonlinear relationship with CCN concentrations. An inflection point is observed around 60 % RH in most cases. Below this level, SHAP values generally increase with increasing RH, suggesting that higher humidity conditions favor aerosol water uptake and enhance CCN activation. Above this level, the SHAP contribution gradually decreases, indicating that the marginal influence of further RH increases on CCN concentrations becomes weaker, possibly because particles have already undergone substantial hygroscopic growth under humid conditions.

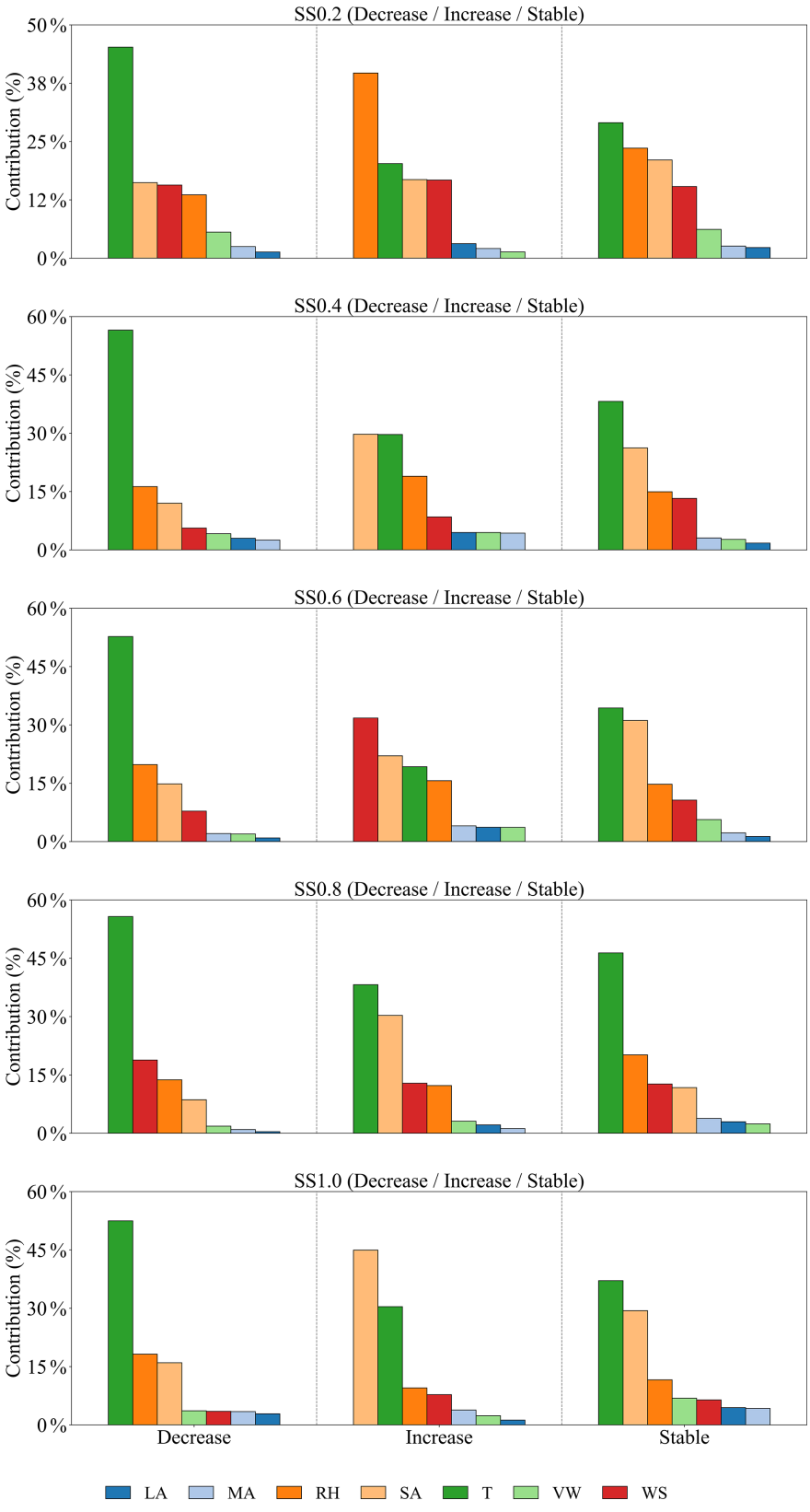

Figure 6. |SHAP| contribution rates of different factors to CCN number concentration under varying aerosol vertical structures and supersaturation conditions. Detailed sample-level SHAP violin summary plots showing the magnitude and direction of individual predictor effects are provided in the Supplement.

The contribution of WS to NCCN SHAP values varies considerably across different scenarios, showing a strong dependence on environmental conditions.

The contributions of other factors show relatively small changes or large variations depending on the scenario, and are therefore not discussed in detail in this study.

4 Conclusions

NCCN reaches up to 10^3 cm^{-3} near the surface and generally decreases with increasing altitude. Under different supersaturation (SS) conditions, the CCN activation fraction exhibits a "first increase–then decrease–then increase" variation with height, reaching a minimum around 4000 m (3 %–8 % for SS $\leq$ 0.6 % and 21 %–35 % for SS $>$ 0.6). Overall, higher activation fractions were observed under SS $\geq$ 0.8, consistent with the expected dependence of CCN activation on supersaturation.

Based on the vertical variation characteristics of aerosol number concentration, the altitude layers are classified into Decrease, Increase, and Stable types, and all segments within each category are combined for statistical analysis. The results show that NCCN differs significantly among different aerosol vertical structures, with the Increase structure exhibiting higher NCCN overall than the Stable and Decrease structures, indicating that aerosol vertical structure may modulate the overall CCN concentration distribution. In contrast, CCN activation ratios do not show a consistent ranking among different vertical structures, but are substantially higher under SS $\geq$ 0.8 %, indicating a stronger dependence on supersaturation.

The CCN-activated droplet spectra generally exhibit a unimodal distribution. At SS = 0.2, the modal diameter is approximately 2 µm, increasing to about 5 µm as SS rises to 1.0. Although the spectral shape is broadly similar across different aerosol vertical structures, with relatively small differences in modal diameter, variations in peak concentration are observed. In general, higher SA correspond to higher CCN peak concentrations.

T, SA, and N_a are consistently positively correlated with CCN, whereas WS, VW, MA, and LA are mainly negatively correlated. RH shows negative correlations under low supersaturation (SS = 0.2 and 0.4) and positive correlations under higher supersaturation (SS = 0.6, 0.8, and 1.0). Overall, T, SA, and N_a exhibit the strongest correlations with CCN, followed by RH and WS, while VW, MA, and LA show weaker correlations. Correlations under the Stable structure are generally weaker than those under the Increase and Decrease structures.

GAM and SHAP analyses indicate that T, SA, RH, and WS are identified as the most important predictors associated with NCCN variations in the model, with contribution rates of approximately 20 %–56 %, 9 %–45 %, 9 %–40 %, and 3 %–32 %, respectively. In the Increase structure, the contribution of T is somewhat reduced. T contributes positively in the Decrease and Increase structures but negatively in the Stable structure. SA contributes positively across all three aerosol vertical structures, whereas WS and RH do not exhibit clear scenario-dependent patterns in their net contributions. In addition, SHAP results show that T, RH, WS, VW, and SA exhibit pronounced nonlinear responses, whereas LA and MA show approximately linear behavior.

The contributions of T and SA generally increase with their magnitude, showing significant positive SHAP contributions at high values. RH exhibits a pronounced nonlinear characteristic, with a turning point around 60 %: below this threshold, SHAP values increase with RH, while above it, they gradually decrease. The contribution of WS varies considerably across different scenarios, showing a strong dependence on environmental conditions. A sensitivity analysis based on a quasi-level flight segment further showed that the importance of temperature decreased after substantially reducing altitude variability, although a positive temperature–NCCN association remained. This indicates that part of the temperature importance in the full dataset is related to altitude-associated covariation, while the remaining relationship should still be interpreted as a statistical association rather than a direct causal effect.

Overall, the dominant roles of temperature and fine aerosol concentration identified in this study are generally consistent with previous observational and numerical studies showing that thermodynamic conditions and aerosol properties jointly regulate CCN activation (Thomas et al., 2024). Unlike previous numerical studies, particularly direct numerical simulations (DNS), which mainly investigate CCN activation under idealized cloud conditions, this study provides aircraft-based observational evidence of CCN variability and its controlling factors under realistic atmospheric environments. These complementary observational results provide useful constraints for improving our understanding of aerosol–cloud interactions.

Several limitations should be acknowledged. First, CCN measurements at different supersaturation levels were conducted sequentially rather than simultaneously, resulting in partial coupling between altitude and supersaturation. Consequently, comparisons among different SS levels may also contain some influence from differences in sampling altitude and flight trajectory. Second, the analyses were based on four aircraft flights conducted within a limited observational period in March 2018. Therefore, the present dataset cannot fully capture seasonal variability, different synoptic regimes, or regional heterogeneity across eastern China. The relationships identified in this study should consequently be interpreted as representative of the atmospheric conditions sampled during these flights rather than as universally applicable characteristics of eastern China. Future studies incorporating aircraft observations from different seasons, synoptic conditions, and regions, together with numerical simulations, are

needed to further evaluate the generality of these findings and the underlying physical mechanisms.

In addition, some predictor variables, particularly temperature and altitude, are physically correlated in aircraft observations. Consequently, although GAM and SHAP identify temperature as one of the most influential predictors, the model quantifies statistical associations rather than direct causal relationships. Future studies incorporating more independent observations and process-based numerical simulations are needed to further distinguish the respective influences of thermodynamic conditions and altitude-related variability.

Despite these limitations, the present results suggest that variations in lower-tropospheric NCCN are closely associated with aerosol loading, thermodynamic conditions, and aerosol vertical structure. The combination of aircraft observations with interpretable machine learning provides an effective framework for identifying the dominant environmental factors associated with CCN variability and offers valuable observational constraints for improving CCN activation parameterizations in cloud-resolving models as well as larger-scale atmospheric models.

Code and data availability. The code and data used in this study are publicly available in the Zenodo repository (Wang, 2026) at https://doi.org/10.5281/zenodo.23387182.

Supplement. The supplement related to this article is available online at https://doi.org/10.5194/acp-26-16325-2026-supplement.

Author contributions. Yichen Lu conducted the conceptualization of the study, performed data curation, formal analysis, validation, and investigation, and was responsible for manuscript preparation, including writing the original draft and revising the manuscript. Honglei Wang contributed to the methodology development, supervised the research, acquired funding, and revised the manuscript. Deyu Liu and Yue Chen contributed to methodology development and software implementation. Chong Peng and Can Song contributed to data curation and provided resources. All authors reviewed and approved the final version of the manuscript.

Competing interests. The contact author has declared that none of the authors has any competing interests.

Disclaimer. Publisher's note: Copernicus Publications remains neutral with regard to jurisdictional claims made in the text, published maps, institutional affiliations, or any other geographical representation in this paper. The authors bear the ultimate responsibility for providing appropriate place names. Views expressed in the text are those of the authors and do not necessarily reflect the views of the publisher.

Acknowledgements. The authors gratefully acknowledge the Weather Modification Centre of Henan Province, Zhengzhou 450000, China, for providing the aircraft observation data used in this study. The authors also express their sincere appreciation to the aircraft observation crew for their dedicated efforts, professional support, and valuable contributions throughout the field campaigns.

Financial support. This study was supported by the Science & Technology Fundamental Resources Investigation Program (Grant no. 2025FY101504), the Key Science and Technology Project of Henan Province (252102321006), and Open Research Fund Project of State Key Laboratory of Atmospheric Environment and Extreme Meteorology.

Review statement. This paper was edited by Lynn M. Russell and reviewed by two anonymous referees.

References

Albrecht, B. A.: Aerosols, Cloud Microphysics, and Fractional Cloudiness, Science, 245, 1227–1230, https://doi.org/10.1126/science.245.4923.1227, 1989.

Annareddy, R. R., Shaik, F. B., Thatapi, B., Chukkaluri, C. R., and Yadiki, N. A.: Source attribution and temporal patterns of surface ozone in a semi-arid region of southern India via GAM and trajectory models, J. Atmos. Sol.-Terr. Phy., 278, 106699, https://doi.org/10.1016/j.jastp.2025.106699, 2026.

Asa-Awuku, A., Sullivan, A. P., Hennigan, C. J., Weber, R. J., and Nenes, A.: Investigation of molar volume and surfactant characteristics of water-soluble organic compounds in biomass burning aerosol, Atmos. Chem. Phys., 8, 799–812, https://doi.org/10.5194/acp-8-799-2008, 2008.

Baumgardner, D., Jonsson, H., Dawson, W., O'Connor, D., and Newton, R.: The cloud, aerosol and precipitation spectrometer: a new instrument for cloud investigations, Atmos. Res., 59–60, 251–264, https://doi.org/10.1016/S0169-8095(01)00119-3, 2001.

Bi, Z., Ye, Z., He, C., and Li, Y.: Analysis of the meteorological factors affecting the short-term increase in O3 concentrations in nine global cities during COVID-19, Atmos. Pollut. Res., 13, 101523, https://doi.org/10.1016/j.apr.2022.101523, 2022.

Borys, R. D., Lowenthal, D. H., Cohn, S. A., and Brown, W. O. J.: Mountaintop and radar measurements of anthropogenic aerosol effects on snow growth and snowfall rate, Geophys. Res. Lett., 30, https://doi.org/10.1029/2002GL016855, 2003.

Cai, Y., Snider, J. R., and Wechsler, P.: Calibration of the passive cavity aerosol spectrometer probe for airborne determination of the size distribution, Atmos. Meas. Tech., 6, 2349–2358, https://doi.org/10.5194/amt-6-2349-2013, 2013.

Chen, Y., Haywood, J., Wang, Y., Malavelle, F., Jordan, G., Partridge, D., Fieldsend, J., De Leeuw, J., Schmidt, A., Cho, N., Oreopoulos, L., Platnick, S., Grosvenor, D., Field, P., and Lohmann, U.: Machine learning reveals climate forcing from aerosols is dominated by increased cloud cover, Nat. Geosci., 15, 609–614, https://doi.org/10.1038/s41561-022-00991-6, 2022.

Faber, S., French, J. R., and Jackson, R.: Laboratory and in-flight evaluation of measurement uncertainties from a commercial Cloud Droplet Probe (CDP), Atmos. Meas. Tech., 11, 3645–3659, https://doi.org/10.5194/amt-11-3645-2018, 2018.

Guo, S. and Xue, H.: The enhancement of droplet collision by electric charges and atmospheric electric fields, Atmos. Chem. Phys., 21, 69–85, https://doi.org/10.5194/acp-21-69-2021, 2021.

Hobbs, P. V. and Rangno, A. L.: Microstructures of low and middle-level clouds over the Beaufort Sea, Q. J. Roy. Meteor. Soc., 124, 2035–2071, https://doi.org/10.1002/qj.49712455012, 1998.

Hou, T., Lei, H., He, Y., Yang, J., Zhao, Z., and Hu, Z.: Aircraft Measurements of the Microphysical Properties of Stratiform Clouds with Embedded Convection, Adv. Atmos. Sci., 38, 966–982, https://doi.org/10.1007/s00376-021-0287-8, 2021.

Jayachandran, V., Nair, V. S., and Babu, S. S.: CCN characteristics over a tropical coastal station during south-west monsoon: observations and closure studies, Atmos. Environ., 164, 299–308, https://doi.org/10.1016/j.atmosenv.2017.06.012, 2017.

Jose, S., Joseph, S., and Lakshmi, N. B.: Satellite based study on the role of Cloud Condensation Nuclei (CCN) and atmospheric thermodynamics in warm cloud evolution, Atmos. Res., 328, 108452, https://doi.org/10.1016/j.atmosres.2025.108452, 2026.

Ke, Y., Wang, H., Yang, Y., Cui, Y., Shen, L., Wu, Z., Liu, S., and Zhao, T.: A case study of aircraft observations of ice cloud microphysical properties over the North China Plain: Vertical distribution, vertical airflow and aerosol–cloud effects, Atmos. Res., 307, 107488, https://doi.org/10.1016/j.atmosres.2024.107488, 2024.

Kerminen, V.-M., Paramonov, M., Anttila, T., Riipinen, I., Fountoukis, C., Korhonen, H., Asmi, E., Laakso, L., Lihavainen, H., Swietlicki, E., Svenningsson, B., Asmi, A., Pandis, S. N., Kulmala, M., and Petäjä, T.: Cloud condensation nuclei production associated with atmospheric nucleation: a synthesis based on existing literature and new results, Atmos. Chem. Phys., 12, 12037–12059, https://doi.org/10.5194/acp-12-12037-2012, 2012.

Khatri, P., Hayasaka, T., Holben, B. N., Singh, R. P., Letu, H., and Tripathi, S. N.: Increased aerosols can reverse Twomey effect in water clouds through radiative pathway, Sci. Rep.-UK, 12, 20666, https://doi.org/10.1038/s41598-022-25241-y, 2022.

Khatri, P., Yoshida, K., and Hayasaka, T.: Aerosol Effects on Water Cloud Properties in Different Atmospheric Regimes, J. Geophys. Res.-Atmos., 128, e2023JD039729, https://doi.org/10.1029/2023JD039729, 2023.

Kleinheins, J., Shardt, N., Lohmann, U., and Marcolli, C.: The surface tension and cloud condensation nuclei (CCN) activation of sea spray aerosol particles, Atmos. Chem. Phys., 25, 881–903, https://doi.org/10.5194/acp-25-881-2025, 2025.

Köhler, H.: The nucleus in and the growth of hygroscopic droplets, T. Faraday Soc., 32, 1152–1161, https://doi.org/10.1039/TF9363201152, 1936.

Lance, S., Nenes, A., Medina, J., and Smith, J. N.: Mapping the Operation of the DMT Continuous Flow CCN Counter, Aerosol Sci. Tech., 40, 242–254, https://doi.org/10.1080/02786820500543290, 2006.

Lance, S., Brock, C. A., Rogers, D., and Gordon, J. A.: Water droplet calibration of the Cloud Droplet Probe (CDP) and in-flight performance in liquid, ice and mixed-phase clouds during ARCPAC, Atmos. Meas. Tech., 3, 1683–1706, https://doi.org/10.5194/amt-3-1683-2010, 2010.

Lawson, R. P.: Effects of ice particles shattering on the 2D-S probe, Atmos. Meas. Tech., 4, 1361–1381, https://doi.org/10.5194/amt-4-1361-2011, 2011.

Lin, P.-H., Wang, S.-H., Klemm, O., and Lin, N.-H.: Separating the Twomey effect and the semi-direct effect in absorbing aerosol environments through the cloud-aerosol mixing ratio, Atmos. Chem. Phys., 26, 2083–2102, https://doi.org/10.5194/acp-26-2083-2026, 2026.

Liu, A., Wang, H., Li, Y., Yin, Y., Li, B., Chen, K., Cui, Y., He, C., and Dai, M.: Distribution Characteristics of Aerosol Size and CCN during the Summer on Mt. Tian and Their Influencing Factors, Atmosphere-Basel, 11, https://doi.org/10.3390/atmos11090912, 2020.

Liu, S., Wang, H., Zhao, D., Zhou, W., Du, Y., Zhang, Z., Cheng, P., Zhao, T., Ke, Y., Wu, Z., and Huang, M.: Measurement report: Aircraft observations of aerosol and microphysical quantities of stratocumulus in autumn over Guangxi Province, China – daylight variation, vertical distribution, and aerosol–cloud interactions, Atmos. Chem. Phys., 25, 4151–4165, https://doi.org/10.5194/acp-25-4151-2025, 2025.

Lundberg, S. M. and Lee, S.-I.: A Unified Approach to Interpreting Model Predictions, Adv. Neur. In., 30, 4765–4774, 2017.

Nair, A. A., Yu, F., Campuzano-Jost, P., DeMott, P. J., Levin, E. J. T., Jimenez, J. L., Peischl, J., Pollack, I. B., Fredrickson, C. D., Beyersdorf, A. J., Nault, B. A., Park, M., Yum, S. S., Palm, B. B., Xu, L., Bourgeois, I., Anderson, B. E., Nenes, A., Ziemba, L. D., Moore, R. H., Lee, T., Park, T., Thompson, C. R., Flocke, F., Huey, L. G., Kim, M. J., and Peng, Q.: Machine Learning Uncovers Aerosol Size Information From Chemistry and Meteorology to Quantify Potential Cloud-Forming Particles, Geophys. Res. Lett., 48, e2021GL094133, https://doi.org/10.1029/2021GL094133, 2021.

Prabhakaran, P., Myers, T. A., Hoffmann, F., and Feingold, G.: Aerosol–cloud interactions in marine low-clouds in a warmer climate, Atmos. Chem. Phys., 26, 5151–5167, https://doi.org/10.5194/acp-26-5151-2026, 2026.

Ren, J., Zou, S., Xu, H., Liu, G., Wang, Z., Zhang, A., Zhao, C., Hu, M., Shang, D., Tang, L., Huang, R.-J., Sun, Y., and Zhang, F.: Machine learning significantly improves the simulation of hourly-to-yearly scale cloud nuclei concentration and radiative forcing in polluted atmosphere, Geosci. Model Dev., 19, 6403–6416, https://doi.org/10.5194/gmd-19-6403-2026, 2026.

Rose, D., Gunthe, S. S., Mikhailov, E., Frank, G. P., Dusek, U., Andreae, M. O., and Pöschl, U.: Calibration and measurement uncertainties of a continuous-flow cloud condensation nuclei counter (DMT-CCNC): CCN activation of ammonium sulfate and sodium chloride aerosol particles in theory and experiment, Atmos. Chem. Phys., 8, 1153–1179, https://doi.org/10.5194/acp-8-1153-2008, 2008.

Rosenberg, P. D., Dean, A. R., Williams, P. I., Dorsey, J. R., Minikin, A., Pickering, M. A., and Petzold, A.: Particle sizing calibration with refractive index correction for light scattering optical particle counters and impacts upon PCASP and CDP data collected during the Fennec campaign, Atmos. Meas. Tech., 5, 1147–1163, https://doi.org/10.5194/amt-5-1147-2012, 2012.

Tao, J., Kuang, Y., Ma, N., Hong, J., Sun, Y., Xu, W., Zhang, Y., He, Y., Luo, Q., Xie, L., Su, H., and Cheng, Y.: Secondary aerosol formation alters CCN activity in the North China Plain, At-

mos. Chem. Phys., 21, 7409–7427, https://doi.org/10.5194/acp-21-7409-2021, 2021.

Thomas, L., Kumar, B., Zuend, A., Hassan-Barthaux, D., and Rao, S. A.: CCN activation in homogeneous isotropic turbulence: Response to particle characteristics and environmental conditions, Atmos. Res., 297, 107095, https://doi.org/10.1016/j.atmosres.2023.107095, 2024.

Twomey, S.: The Influence of Pollution on the Shortwave Albedo of Clouds, J. Atmos. Sci., 34, 1149–1152, https://doi.org/10.1175/1520-0469(1977)034<1149:TIOPOT>2.0.CO;2, 1977.

Wang, H.: Code and data for vertical structure and controlling factors of cloud condensation nuclei activation over eastern China: Insights from aircraft measurements and interpretable machine learning, Zenodo [code and data set], https://doi.org/10.5281/zenodo.23387182, 2026.

Wang, N., Wang, Y., Lu, C., Zhu, B., Yan, X., Sun, Y., Xu, J., Zhang, J., and Shen, Z.: Interpretable ensemble learning unveils main aerosol optical properties in predicting cloud condensation nuclei number concentration, Npj Clim. Atmos. Sci., 8, 302, https://doi.org/10.1038/s41612-025-01181-y, 2025.

Xu, X., Yin, J., Zhang, X., Xue, H., Gu, H., and Fan, H.: Airborne measurements of cloud condensation nuclei (CCN) vertical structures over Southern China, Atmos. Res., 268, 106012, https://doi.org/10.1016/j.atmosres.2021.106012, 2022.

Zhang, M., Deng, X., Zhu, R., Ren, Y., and Xue, H.: The Impact of Aerosol Vertical Distribution on a Deep Convective Cloud, Atmosphere-Basel, 12, https://doi.org/10.3390/atmos12060675, 2021.

Zhang, R., Wang, Y., Li, Z., Wang, Z., Dickerson, R. R., Ren, X., He, H., Wang, F., Gao, Y., Chen, X., Xu, J., Cheng, Y., and Su, H.: Vertical profiles of cloud condensation nuclei number concentration and its empirical estimate from aerosol optical properties over the North China Plain, Atmos. Chem. Phys., 22, 14879–14891, https://doi.org/10.5194/acp-22-14879-2022, 2022.

Zhao, C., Qiu, Y., Dong, X., Wang, Z., Peng, Y., Li, B., Wu, Z., and Wang, Y.: Negative Aerosol-Cloud re Relationship From Aircraft Observations Over Hebei, China, Earth and Space Science, 5, 19–29, https://doi.org/10.1002/2017EA000346, 2018.

Zhao, C., Sun, Y., Yang, J., Li, J., Zhou, Y., Yang, Y., Fan, H., and Zhao, X.: Observational evidence and mechanisms of aerosol effects on precipitation, Sci. Bull., 69, 1569–1580, https://doi.org/10.1016/j.scib.2024.03.014, 2024.

Zipfel, L., Andersen, H., Grosvenor, D. P., and Cermak, J.: How Cloud Droplet Number Concentration Impacts Liquid Water Path and Precipitation in Marine Stratocumulus Clouds – A Satellite-Based Analysis Using Explainable Machine Learning, Atmosphere-Basel, 15, https://doi.org/10.3390/atmos15050596, 2024.